[American Journal of Science, Vol. 309, September, 2009, P. 607–632, DOI 10.2475/07.2009.04]

INTERACTION BETWEEN PRESSURE SOLUTION AND CLAYS IN STYLOLITE DEVELOPMENT: INSIGHTS FROM MODELING

EINAT AHARONOV and REGINA KATSMAN

The Hebrew University of Jerusalem, The Institute of Earth Sciences, Givat Ram, Jerusalem, 91904, Israel; einatah@cc.huji.ac.il, reginak@savion.huji.ac.il

ABSTRACT. Stylolites are localized dissolution surfaces commonly found in sedimentary rocks. Stylolites have been extensively studied due to their important role in controlling dissolution, precipitation, deformation, and fluid transport in rocks. Field observations indicate that stylolite formation and morphology are strongly correlated both with the surrounding stress and with the distribution of clays within the host rock, yet the mechanism by which they form remains enigmatic. We present results from a newly developed two-dimensional Spring-Network Model that studies stylolite formation by pressure-solution with and without the presence of clays, where clays play a role of enhancing pressure solution. We use our model to test the relative role of stress and clays in controlling the localization of dissolution into stylolites. In contrast to the common paradigm, our results suggest that pressure solution alone, in the absence of catalyzing clays, does not lead to spontaneous localization of dissolution into stylolites. Instead, we propose a new coupled clay-pressure-solution feedback to localize stylolites, a coupling that we observe in our model: a region with a slightly larger clay fraction will experience enhanced dissolution, and will thus accumulate more residual clays, which will act to further enhance pressure solution in that region, and accumulate even more clays. Stress is a necessary component in this feedback as it controls the direction of stylolite propagation, and facilitates lateral propagation.

Keywords: Stylolites, pressure solution, clays, spring network model

INTRODUCTION

Stylolites are localized dissolution surfaces abundantly found in carbonate and sandstone rocks, and also in other sedimentary and metamorphic rocks. They often account for a large degree of dissolution. In some cases more than 50 percent of the original rock volume has been removed by dissolution at stylolites (Stockdale, 1922; Alvarez and others, 1978). Material dissolved at stylolites provides cement and thus often controls porosity reduction in the host rocks (for example Heald, 1956; Ehrenberg, 1990). Stylolites play a crucial role in controlling the quality of hydrocarbon reservoir rocks, and the process of their formation has large economical implications (for example Ehrenberg, 2006) as well as geological implication (for example Marshak and Engelder, 1985).

Stylolites are marked by a rough suture ($1\mu m - 1$ *cm* thick) filled by an insoluble residue of clay, oxides, and/or organic matter. Figure 1A shows a typical example of a stylolite. Already Stockdale (1922) noted that in stylolites from diverse origins, locations and tectonic settings, the amount of dissolved rock, W, decreases gradually from a maximum, $W_{\max}$, at the center of the seam to zero at its periphery. Mardon (ms, 1988) reports that sets of carbonates solution seams from the Valley and Ridge formation in Pennsylvania have constant maximum width, $W_{\max}$, to length, L, aspect ratios, so that, $W_{\max}/L = const.$ It was thus inferred that stylolites often start from a seed and propagate sideways and at the same time undergo continued dissolution on their flanks (for example Fletcher and Pollard, 1981; Safaricz and Davison, 2005). It should be noted however that in contrast to laterally growing stylolites, other stylolites are believed to localize on preexisting clay laminas (Walderhaug and Bjørkum, 2003), in which case the extent of the clay lamina originally present determined their lateral extent.

Since their first description by Mylius in 1751, the mechanism of stylolite formation was hotly debated (see for example Bathrust, 1971). Stylolites have never been

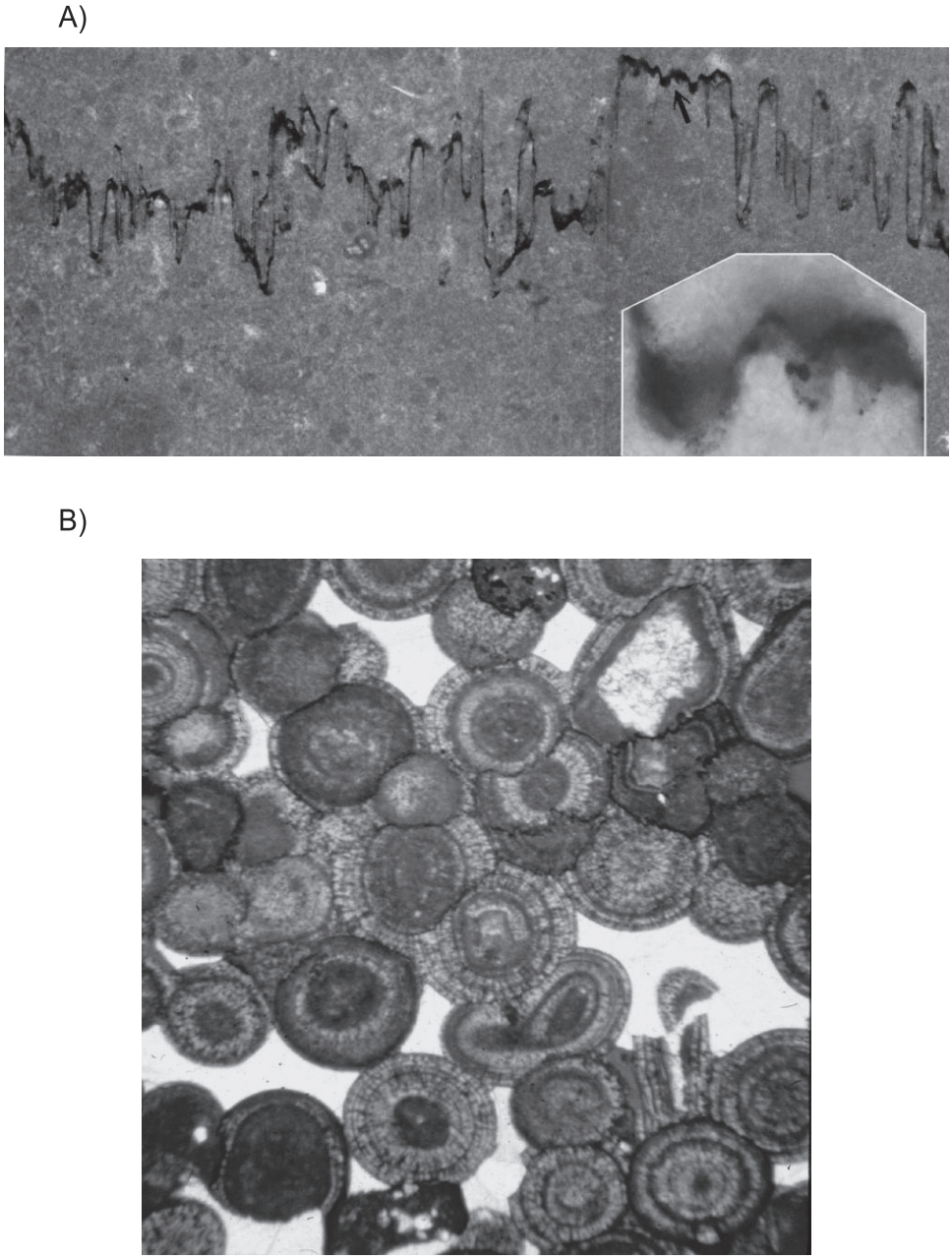

Fig. 1. (A) A photo of a typical stylolite from Devonian intraclastic micstone to packstone, field of view is about 7.0 mm wide. The stylolite seam is dark due to filling of insoluble clays. Taken from Atlas of Pressure Dissolution Features, by L. B. Railsback, http://www.gly.uga.edu/railsback/PDFimage0204a.html. (B) An Oolithoc limestone, Smackover formation, Walker Creek field, Louisiana, picture courtesy of David Budd, Colorado University. The initially spherical oolites experienced a large degree of pressure solution, as seen by grain interpenetration. The white infilling of the pore space is carbonate cement, most likely originating from the dissolved contacts. Free faces of grains are intact and not dissolved, indicating the role of stress in the dissolution process. The highly dissolved grain contacts form a connected path along which stress is transmitted across the sample.

produced in the lab (except on the sub-grain scale by Gratier and others, 2005), and the physics of their evolution is not well understood. The debate is still ongoing with several leading suggestions:

1. Stylolites are produced by spontaneous localization of 'pressure solution' (PS) in an otherwise uniform rock (for example Merino and others, 1983; Dewers and Ortoleva, 1990). An important hypothesis is that stylolites are anti-cracks that propagate via a feedback controlled by the stress field they create (Fletcher and Pollard, 1981).
2. Stylolites originate at clay-rich lamina (Walderhaug and Bjørkum, 2003), resulting from clay-enhanced dissolution, a process that is not well understood (Bjørkum, 1996; Oelkers and others, 1996; Walderhaug and others, 2004, 2006).
3. Stylolites form by PS, but clays are an important part of the process. Clays are known from field observations to play an essential role in the PS process (for example Heald, 1956; Thomson, 1959; Oldershaw and Scoffin, 1967; Sibley and Blatt, 1976; Bayly, 1986). Experiments also show that clays enhance PS rates considerably (Hickman and Evans, 1991; Renard and others, 1997, 2001; Alcantar and others, 2003; Meyer and others, 2006; Greene and others, 2009). There are many observations that the clay distribution and content affects the degree of PS localization (for example Heald, 1956; Marshak and Engelder, 1985). Yet there are very few quantitative models that incorporate clays into the physics of stylolite formation (Fueten and Robin, 1992; Fueten and others, 2002).
4. Some stylolites are linked to the presence of organic matter and form under low pressure, very early in the diagenetic history of sedimentary rocks (Gruzman, ms, 1997).

Despite the offered insights, and the importance of the problem, a coherent picture of the process of stylolite formation is still missing.

The aim of this work is to offer a systematic set of numerical experiments, to test and compare the different leading hypotheses for the formation of stylolites as detailed above, and to finally formulate a new hypothesis. We use a new two-dimensional numerical technique based on our previous works (Katsman and others, 2005, 2006a; Katsman and Aharonov, 2006) to study stylolite formation in an initially nearly uniform rock. The model systematically studies whether PS alone, clay-induced dissolution by itself (without the aid of stress), or a coupling between PS and various mechanisms by which clays may enhance dissolution, may be responsible for spontaneous localization of dissolution. Specifically we investigate here the physics of situations in which dissolution occurs as intergranular PS, and spontaneously localizes into a sub-planar propagating defect, forming a stylolite that continuously dissolves along its flanks, as well as continues to propagate sideways.

We consider stylolite propagation and growth to be a basic question, similar to that of the crack growth. Stylolite roughness and stylolites spacing, similar to crack roughness and crack spacing, are also very important (for example Railsback, 1998; Koehn and others, 2007; Ebner and others, 2009), but will be addressed by us at a later stage, once the basic mechanisms controlling stylolite elongation and thickening are determined.

STRESS AND CLAY INDUCED DISSOLUTION— OVERVIEW

This section reviews current understanding of stress and clay-induced dissolution, focusing on inter-granular dissolution.

Kinetics of Inter-granular Pressure Solution

The role of stress in controlling chemically facilitated compaction of granular and porous rocks is well documented (for example Paterson, 1973, 1995; De Boer, 1977; Shimizu, 1995; Lehner, 1995). Figure 1B is an example of a grain-rock where the initially spherical oolites show evidence of a large amount of PS at grain contacts resulting in grain interpenetration. Free faces of grains are intact and not dissolved, as expected from grains exposed to a pore space with hydrostatically stressed fluids. The dissolved contacts form a connected path indicating stress transmission across the sample. Such high-stress paths, in the language of granular matter, are termed 'stress chains'. The similarity between stress chains in granular simulations (for example Radjai and others, 1998; Aharonov and Sparks, 1999) and the connected path of grains with a high degree of PS at their contacts, agrees with the commonly held understanding of the connection between dissolution at the grain contacts and the stress on them.

There are three mechanisms suggested for intergranular PS: Thin-film PS (Weyl, 1959; Rutter, 1976), Undercutting PS (Tada and Siever, 1989; Karcz and others, 2006), and Channel and Island PS (Bathrust, 1971; Tada and others, 1987). For a review on the mechanisms see De Meer and Spiers (1999). The driving force for PS arises from spatial variations in the chemical potential along grain surfaces. Dissolution occurs at sites of high chemical potential, followed by transfer of solute through the fluid phase, and then precipitation at regions with a lower chemical potential. Variations in the chemical potential, $\Delta\mu$, arise due to spatial variations in stress, plastic and elastic strain energies, crystal orientation, and interface curvature (Paterson, 1973, 1995; De Boer, 1977; Shimizu, 1995; Lehner, 1995). Lehner (1995) computed inter-granular PS rates from thermodynamic considerations, and the reader is directed to that paper for full details. The rate of grain-to-grain convergence $\dot{\varepsilon}$ is given there in equation (18), as a function of the overall driving force for the process, defined as the difference between the average normal component of solid-phase chemical potential at grain contacts $\tilde{\mu}_s^{ch}$ and the chemical potential at the free pore-grain interface μ_a^{ch}.

$$\dot{\varepsilon} = -K^{eff}(\tilde{\mu}_s^{ch} - \mu_a^{ch}) = -K^{eff}\Delta\mu^{ch} \tag{1}$$

The potential difference $\Delta\mu^{ch} = \tilde{\mu}_s^{ch} - \mu_a^{ch}$ represents the average total driving force for the combined process of inter-granular dissolution and grain-boundary diffusion. Here we took the liberty to change the notation of Lehner (1995), substituting the collection of material constants (eq 18 there) that multiply the driving force, $\Delta\mu^{ch}$, by an effective rate constant for the process, K^{eff}. This substitution allows focusing on the essential ingredients in equation (1): the thermodynamic driving force, $\Delta\mu^{ch}$, and the effective rate constant, K^{eff}. From hereon we focus on thin-film PS, since this process has the largest driving force. However the modeling results can be easily generalized to other PS mechanisms.

According to Lehner (1995), when the PS process is limited by diffusion within the thin film:

$$K^{eff} = \frac{8D^{gb}\delta_0}{a^2 l^{eq}}\,\rho^f C_0^{eq}\frac{\Omega}{RT} \tag{2}$$

Where ρ^f is the mass density of fluid phase, δ_0 is the thin-film thickness, l^{eq} the distance between grains centers, a is the radius of the grains contact, calculated as shown in the Appendix, D^{gb} is the grain boundary diffusivity through the thin film, C_0^{eq} is the reference equilibrium concentration under an isotropic pressure P, Ω is molar volume of the solid phase, R is the universal gas constant, and T is the absolute temperature. Parameters are summarized in table 1.

Table 1

Parameters and units of the calculations

Parameter	*Definition*	*Value (Unit)*
a	Grain contact radius	(m)
C_0^{eq}	Reference equilibrium Quartz concentration under an isotropic pressure P	10^{-4} (mass fraction)
l_0^{eq}	Initial grain diameter	$5 \cdot 10^{-4}$ (m)
l^{eq}	Truncated grain diameter	$4.55 \cdot 10^{-4}$ (m)
D^{gb}	Grain boundary diffusivity; $D^{gb} = 0.1D$	(m^2 / s)
D	Molecular diffusivity; $D = D_0 \exp(-15000 / RT)$	(m^2 / s)
D_0	Reference molecular diffusivity	$9 \cdot 10^{-7} (m^2 / s)$
E	Young's modulus of Quartz	19 (GPa)
K^{eff}	Effective dissolution rate constant	(m / s)
P	Pore pressure	0 (Pa)
R	Universal gas constant	8.314 $(J / (mol \cdot K))$
T	Absolute temperature	390 (K)
Ω	Molar volume of quartz	$2.27 \cdot 10^{-5} (m^3 / mol)$
δ_0	Thin-film thickness without presence of clays	$2 \cdot 10^{-9}$ (m)
δ	Contact thickness in presence of clays	$6.8 \cdot 10^{-6}$ (m)
V^{cont}	Volume fraction of clays within a contact	(unitless)
V_{crit}^{cont}	Critical volume fraction of clays within a contact	0.8
ρ^s	Mass density of solid phase	2650 (kg/ m^3)
ρ^f	Mass density of fluid phase	1000 (kg/ m^3)
$\Delta\mu^{ch}$	Chemical potential difference	(m^2 / s^2)
$\Delta\mu^{el}$	Electrical potential difference	(m^2 / s^2)

Assuming that the pore-fluid is saturated with respect to the free grain-surface, the difference in chemical potential (the overall average driving force) [Lehner (1995), eq 22] for the combined process of inter-granular dissolution and grain-boundary diffusion, is:

$$\Delta\mu^{ch} = \tilde{\mu}_s^{ch} - \mu_a^{ch} = (\sigma^n - P)/\rho^s \tag{3}$$

Here σ^n is the average normal stress on the contact, P is the pore fluid pressure, and ρ^s is the mass density of solid phase. The strain-energy term of the chemical potential is neglected in the driving force, as it is calculated to be much smaller than the stress driving force in equation (3).

Review of the Role of Clays in Chemical Compaction

In addition to the many papers dealing with the role of stress in controlling PS and grain convergence, many field observations and lab experiments point to the important role of clays and phyllosilicates in enhancing chemical compaction, although the mechanism by which they enhance dissolution is not completely clear. Field observations start with Heald (1956) who found an inverse relation between porosity and clay content in St. Peter Sandstone, and attributes porosity loss to clay-enhanced pressure solution. Thomson (1959) noted the high occurrence of clay in zones of massive

chemical compaction. Sibley and Blatt (1976) used Cathodo-luminescence to show that the presence of clay between grains was one of the most important variables correlated with extensive chemical compaction. Chemical compaction occurring at very shallow burial depths and very low stress has also been reported by Railsback (1993) and Gruzman (ms, 1997). Bjørkum (1996) and Oelkers and others (1996) present textural observations of quartz dissolution at mica-quartz interfaces in sandstones. Using Cathodo-luminescence imaging and other techniques they found that whenever evidence of grain-to-grain quartz dissolution is observed, illitic clays are present at the interface. Bjørkum (1996) suggested that what has been considered to be a PS process, may be a clay-induced or clay-enhanced dissolution process. This view is in contrast to other suggestions that clays do not necessarily play a catalyzing role and may be a mere residue (for example Andrews and Railsback, 1997).

Experimental observations indicating that clays play an active and important role in chemical compaction include:

1. Increase in chemical compaction rate with increasing clay content mixed within aggregates of halite (Renard and others, 1997, 2001);
2. Experiments on synthetic mixtures of quartz sand and fine grained illite + muscovite compacted at a range of effective pressures and temperatures, show dramatically faster compaction rates compared to control experiments in clean sand (without illite or muscovite)—about 100 times faster (Rutter and Wanten, 2000);
3. Addition of clay minerals to carbonate ooze samples subjected to pressures and temperatures retarded the rate of recrystallization by chemical compaction (Baker and others, 1980);
4. Experiments on halite single crystals loaded in brine showed a fivefold increase in convergence rates in experiments conducted with a film of Na-montmorillonite coating the halite compared to experiments conducted without mica coating (Hickman and Evans, 1995).

Based on the above observations it is reasonable to suggest that PS may often be influenced by the presence of clays at grain contacts. However, there is no consensus concerning the mechanism by which clay affects dissolution, whether it changes reaction kinetics (Renard and others, 2001; Sheldon and others, 2003), or changes thermodynamic driving force (Bjørkum, 1996; Oelkers and others, 1996; Walderhaug, 2004, 2006; Greene and others, 2009). These mechanisms are discussed below.

Kinetic mechanism.—Renard and others (2001) and Sheldon and others (2003) proposed that clay particles prop open contacts between dissolving particles. In this way clays enlarge the film thickness δ (fig. 2), and enhance dissolution rates under diffusion-controlled thin-film PS, by increasing K^{eff} in equation (2). The strain rate (grain convergence rate) is then expected to increase according to equation (1).

Thermodynamic mechanism.—Another option is that contact with clays actually increases the solubility of minerals, rather than changing K^{eff}. Walderhaug and others (2004) and Oelkers and others (1996) suggested that clays enhance local quartz solubility by changing *pH*. An interesting recent suggestion (Walderhaug and others, 2006) builds upon basic thermodynamic considerations (Gibbs) that contact between surfaces with different surface charges (for example between quartz and clay) gives rise to an electrochemical potential in the water film that exceeds the chemical potential of mineral surfaces exposed directly to pore fluid. Subsequently, an electrochemical potential difference between the water film and adjacent pores drives dissolution at the contact and re-precipitation on the free mineral interface. Walderhaug and others (2006) used a generalized electrochemical potential, μ^g, consisting of chemical, μ^{ch}, and electric, μ^{el} potentials, as following:

$$\mu^g = \mu^{ch} + \mu^{el} \tag{4}$$

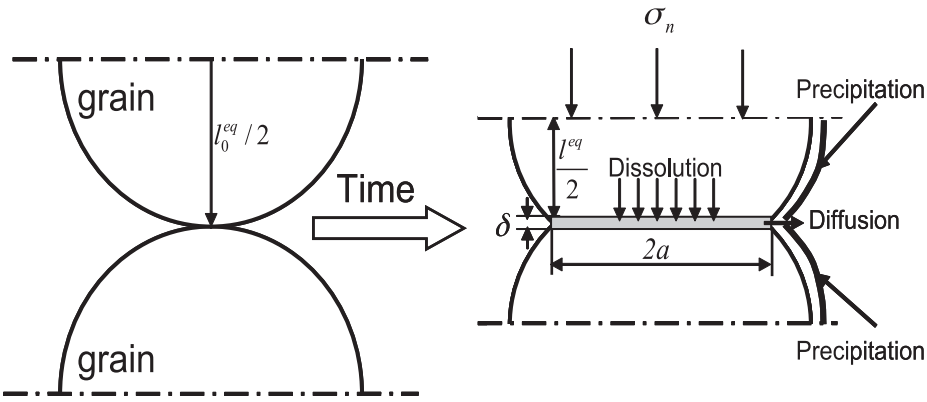

Fig. 2. Two identical spherical grains undergoing dissolution at their contact, with $l_0^{eq}/2$ the initial radius of the grains. After dissolution, the grain centers converge, with l^{eq} the new distance between grains centers. As the grain dissolve at their contact, the contact radius a increases. Here a thin-film of thickness δ_0 is assumed to exist at the contact (δ is the contact thickness, which in the presence of clay may be different from δ_0), and σ_n is the stress acting perpendicular to the grain contact.

where the electric potential, μ^{el}, depends on the surface charge density of the two grains pressed against each other. In order to test this hypothesis, Greene and others (2009) experimentally studied dissolution of quartz and silica brought into contact with dissimilar minerals with a thin fluid film separating the two surfaces. In addition, an external potential field was induced to further test the hypothesis that electric potentials enhance dissolution. Dissolution rate was found to depend strongly on the electric potential between the contacting minerals (Greene and others, 2009). From this they infer that when illitic clay or micas are pressed against quartz or calcite, the large surface charge of these phases profoundly affects the charge balance at the soluble mineral surfaces and thus increase their solubility (De Meer and others, 2002; Alcantar and others, 2003; Meyer and others, 2006; van Noort and others, 2007). It is clear that stress also plays a large role in this process—by controlling the thickness of the water film and the degree of mineral interaction.

NUMERICAL MODEL

In order to study stress-induced and clay-induced dissolution in elastic media, we utilize the spring network model (SNM) that has been used extensively to investigate crack propagation (Curtin and Scher, 1990a, 1990b), and adopted by us recently to model irreversible localized volume reduction phenomena (LVR) in elastic media, specifically mechanical and chemical compaction (Katsman and others, 2005, 2006a, 2006b; Katsman and Aharonov, 2006). The model is composed of two main components: Elastic and Chemical Compaction. The model will be used as an experimental tool: to investigate the physics of different dissolution processes and compare the outcome.

Elastic Component

Elastic matter is represented in our model by a two-dimensional hexagonal lattice, with nodes linked by linear elastic Hookian springs (fig. 3A). Springs are characterized by their Young's modulus, E_{ij}, and their cross-sectional area, A_{ij}. The force at spring connecting nodes ***i-j***, is determined by its length l_{ij} departure from its equilibrium length l_{ij}^{eq} according to:

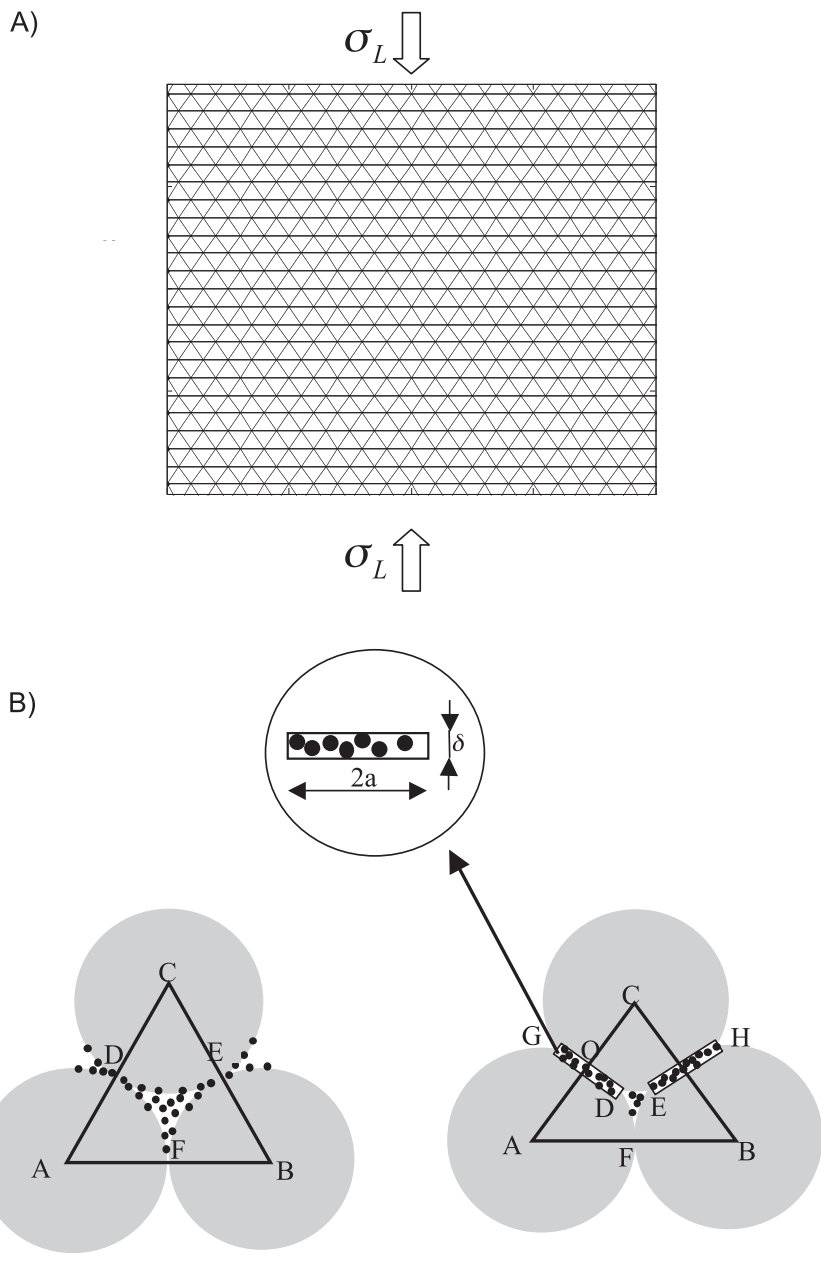

Fig. 3. (A) Elastic matter is represented in the simulations as a two-dimensional hexagonal lattice, where nodes are linked by linear elastic Hookian springs. Stress boundary conditions are applied to the horizontal boundaries, while the vertical boundaries remain free. (B) The symmetrical triangular unit of three springs (ABC) is considered as the basic unit for calculations, with the grain centers located at the unit tips. Each spring represents the distance between the centers of two grains in contact, where the grain contact transmits the normal stress measured on the spring. It is also assumed that within the unit, free grain surfaces are exposed to a pore fluid with a pressure P. Grains dissolve at the contact and grain centers converge. Black dots represent insoluble matter, such as clay. Clay accumulates at the grains contacts as dissolution proceeds (in rectangle GD and EH of size $2a \times \delta$, inset), as calculated in the Appendix.

$$F_{ij} = F_{ji} = -\alpha_{ij}(l - l^{eq})_{ij} \qquad \alpha_{ij} = \frac{E_{ij}A_{ij}}{l_{ij}^{eq}} \tag{5}$$

Here, positive (negative) forces correspond to contracted (stretched) springs respectively. Our calculations require the normal stress on the spring, σ_{ij}, which is the force divided by the cross sectional area, A_{ij}. Simulations start from a relaxed equilibrium lattice position, with neither boundary nor internal nodes displacements (fig. 3A). Then strain or stress boundary conditions are applied to the horizontal and vertical boundaries, and the new equilibrium position for each internal and boundary node is found.

Although in principle the springs may represent any chosen length (a unit of rock or a single grain), in this paper each spring represents the distance between centers of neighboring grains (fig. 3B). However, the resultant dissolution usually lacks granular structure and propagates at the interface between grains. The hexagonal spring array describes a hexagonal packing of grains. To avoid lattice artifacts (Curtin and Scher, 1990a, 1990b), the symmetric triangular unit of three springs is considered as the basic unit for calculations. Each such unit, shown in figure 3B, represents a small volume where the grains' centers are located at the unit's tips.

Chemical Compaction Component

In Katsman and others (2005, 2006a) we developed a variation of the basic SNM, which allows modeling irreversible strain induced by mechanical or chemical compaction. Irreversible strain is modeled by a decrease in the spring's equilibrium length l_{ij}^{eq} (fig. 2) in response to compressive stress or other factors (Katsman and others, 2006a, 2006b). However the law by which l_{ij}^{eq} evolves is different for different physical processes. Our previous works (Katsman and others, 2005; Katsman and Aharonov, 2006) modeled mechanical compaction using springs that represent a macroscopic unit of rock (and not single grains as here) and a mechanical yield criteria: In springs that experienced a compressive normal stress larger than a prescribed threshold, the equilibrium length abruptly shortened, thus simulating grain crushing, rearrangement and resultant porosity reduction. The mechanical compaction model was used to study compaction band nucleation, evolution, and interaction with other defects (Katsman and others, 2005, 2006a, 2006b; Katsman and Aharonov, 2006). That model provided an innovative tool that allowed gaining insights into the complex physics of compaction defect propagation.

A variation on the mechanical yield procedure is proposed here to model chemical compaction. For simplicity (but with no loss of generality) it is proposed to first run simulations where each spring connecting nodes **i-j** represents the distance between the centers of two grains (**i** and **j**) in contact (fig. 3B), where the grain contacts transmit the normal stress measured on the spring. The pores and contacts are filled with saturated fluid. The equilibrium length, l_{ij}^{eq}, may continuously shorten (see eq 1), via dissolution at the grains contacts (fig. 2):

$$\dot{\varepsilon}_{ij} = \frac{1}{l_{ij}^{eq}} \frac{\Delta l_{ij}^{eq}}{\Delta t} = -K_{ij}^{eff} \Delta \mu_{ij}^{g} \tag{6}$$

Where $\Delta\mu_{ij}^{g} = \Delta\mu_{ij}^{ch} + \Delta\mu_{ij}^{el}$ is a generalized electrochemical potential difference (the definition for μ_{ij}^{g} is presented in eq 4) at the contact i-j. The chemical potential difference $\Delta\mu_{ij}^{ch}$ between the grain contacts and the free pore-grain interface, is presented in equation (3). The electric potential difference $\Delta\mu_{ij}^{el}$ between the grain contacts and at the free pore-grain interface will be discussed later in this section. In the absence of any electrical effects (here arising only from the presence of clays at the

contact) $\Delta\mu_{ij}^{g}$ is reduced to $\Delta\mu_{ij}^{ch}$ in equation (3). As l_{ij}^{eq} continuously shrinks during dissolution (figs. 2 and 3B), the contact radius, a_{ij}, grows. The evolving value of a_{ij} is used in calculating K_{ij}^{eff} from equation (2). The dependence of K_{ij}^{eff} and $\Delta\mu_{ij}^{g}$ on variables such as stress, clay content, or strain energy encapsulates the kinetics and the thermodynamic driving forces respectively. In this paper we test several different functions proposed in the literature for $\Delta\mu^{g}$ and K^{eff} to investigate chemical compaction in general and stylolite localization in particular.

Transport between the pores is assumed to be rapid compared to inter-granular chemical compaction rates, an assumption valid for systems smaller than the transport length (for example as in Fueten and Robin, 1992; Fueten and others, 2002) leading to a uniform μ_{a}^{ch} in the system. Alternatively, this assumption is valid for an open system with fluid composition controlled by external fluid flow. This assumption will be relaxed in future works, where we plan to add fluid transport on a grid placed on top of the elasto-plastic deforming matrix. Another approximation we make is that precipitation occurs in the open pores between the grains but does not change the grain shapes considerably. This is a good approximation for the initial stages of dissolution.

We simulate Thin-Film diffusion-controlled PS in granular rocks, with and without clays. Two types of initial condition for simulations are used: a "clean" rock with grains composed of a single mineral and no clays, and a "dirty" rock with a small amount of clay, V_0, initially uniformly distributed along grain interfaces and in the pores (fig. 3B). Clay is treated as an insoluble residue. As grains dissolve, the radius a_{ij} of grain contacts increases, and pores shrink. The volume fraction that the insoluble clays occupy increases within the grain contacts and the pores as dissolution proceeds (fig. 3B). The evolution of clay volume fraction within grain contacts, V_{ij}^{cont}, is calculated during dissolution, as detailed in the Appendix.

Since the mechanism by which clays influence dissolution is not yet clear, the two proposed mechanisms for clay influence on dissolution are studied separately:

Kinetic mechanism.—In this mechanism the reaction rate constant, K_{ij}^{eff}, in equation (6) increases as function of the clay volume fraction. As suggested above, clays may increase K_{ij}^{eff} by increasing contact thickness δ (eq. 2) (Renard and others, 2001). It seems likely that in order to elevate K_{ij}^{eff} a nearly continuous coverage of clays on the grain contact is required. We thus assume for simplicity a step function of K_{ij}^{eff} vs. V_{ij}^{cont} (fig. 4A). If the clay volume fraction within grain contacts is larger than a prescribed critical value $V_{ij}^{cont} \geq V_{crit}^{cont}$ then $K_{ij}^{eff} = \alpha K_{clean}^{eff}$ with $\alpha \gg 1$ taken as a constant (fig. 4A), where the base dissolution rate in a clean system K_{clean}^{eff} is calculated according to equation (2).

Thermodynamic mechanism.—In this mechanism clays increase the electrochemical potential, as described in the *Review of the Role of Clays in Chemical Compaction* section. To fully model this mechanism requires understanding *how* clays affect the electrochemical potential, but this is unfortunately not yet known (Greene and others, 2009). Nevertheless, modeling of the essential features of the process, even without the specific details, will help gain insight. Therefore an approximation of a new generalized potential difference $\Delta\mu_{ij}^{g}$ (eq 6) is offered. $\Delta\mu_{ij}^{g}$ at each contact is the sum of the chemical potential difference $\Delta\mu_{ij}^{ch}$ (eq 3), and an electric potential difference $\Delta\mu_{ij}^{el}$ between the grain contacts and at the free pore-grain interface (see eq 4 here, see Walderhaug and others, 2006).

We assume that elevation of $\Delta\mu_{ij}^{el}$ requires a nearly continuous coverage of clays on the grain contact. In modeling it is assumed that if the clay volume fraction, V_{ij}^{cont} (see Appendix), within grain contacts is below a certain threshold, the electric potential difference between the grain contact and the free face, $\Delta\mu_{ij}^{el}$, is zero. If $V_{ij}^{cont} \geq V_{crit}^{cont}$ $\Delta\mu_{ij}^{el}$ attains a new, higher value, as demonstrated in figure 4B.

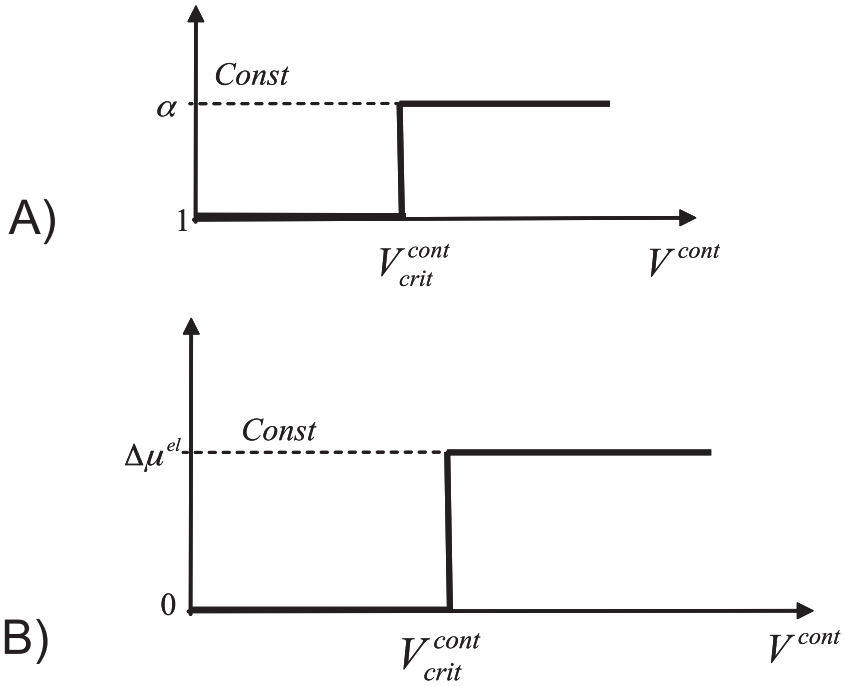

Fig. 4. Clays accumulate within the contact, and their volume fraction increases. If the volume fraction of clay, V^{cont}, within the grain contacts (within a rectangle of size $2a \times \delta$, fig. 3B) is smaller than a prescribed critical value, V^{cont}_{crit}, clays are considered to have no influence on the dissolution process. Once clays exceed a critical fraction, $V^{cont} \geq V^{cont}_{crit}$, the kinetics or the driving forces are altered: (A) In the kinetic mechanism clays alter the effective reaction rate constant, K^{eff}. If $V^{cont} \geq V^{cont}_{crit}$, then the effective rate increases α-fold, so that $K^{eff} = \alpha K^{eff}_{clean}$ with $\alpha \gg 1$. (B) In the electro-chemical mechanism clays alter $\Delta\mu^{el}$. Once $V^{cont} \geq V^{cont}_{crit}$, a new constant elevated value for the electric potential difference $\Delta\mu^{el} = const$ is used.

As a result the generalized electrochemical potential difference used in this case is:

$$\Delta\mu^{g}_{ij} = \frac{(\sigma^{n}_{ij} - P)}{\rho^{s}} + \Delta\mu^{el}_{ij} \tag{7}$$

Modeling Procedure

Our modeling procedure is outlined below (see fig. 5):

1. *Step 0:* The simulations are initiated either with no clays (a "clean" rock) or with a uniform distribution of clays (a "dirty" rock). Simulations start with a small seed defect that has undergone a small amount of dissolution (fig. 6). The simulations are then run by looping over the following steps:
2. *Step I:* The normal stress σ^{n}_{ij} on each spring representing a grain contact is calculated based on a force equilibrium in each node of the entire spring network (as detailed in Katsman and others, 2005, 2006a).
3. *Step II:* Based on the stress and the volume fraction of clays within each contact, V^{cont}_{ij}, and depending on the assumed mechanism for clay enhanced dissolution, we calculate the driving force for dissolution, $\Delta\mu^{g}_{ij}$, and the reaction rate constant in each spring, K^{eff}_{ij}.
4. *Step III:* Using $\Delta\mu^{g}_{ij}$ and K^{eff}_{ij}, the rate of grain convergence, $\dot{\varepsilon}_{ij}$, is derived from equation (6).

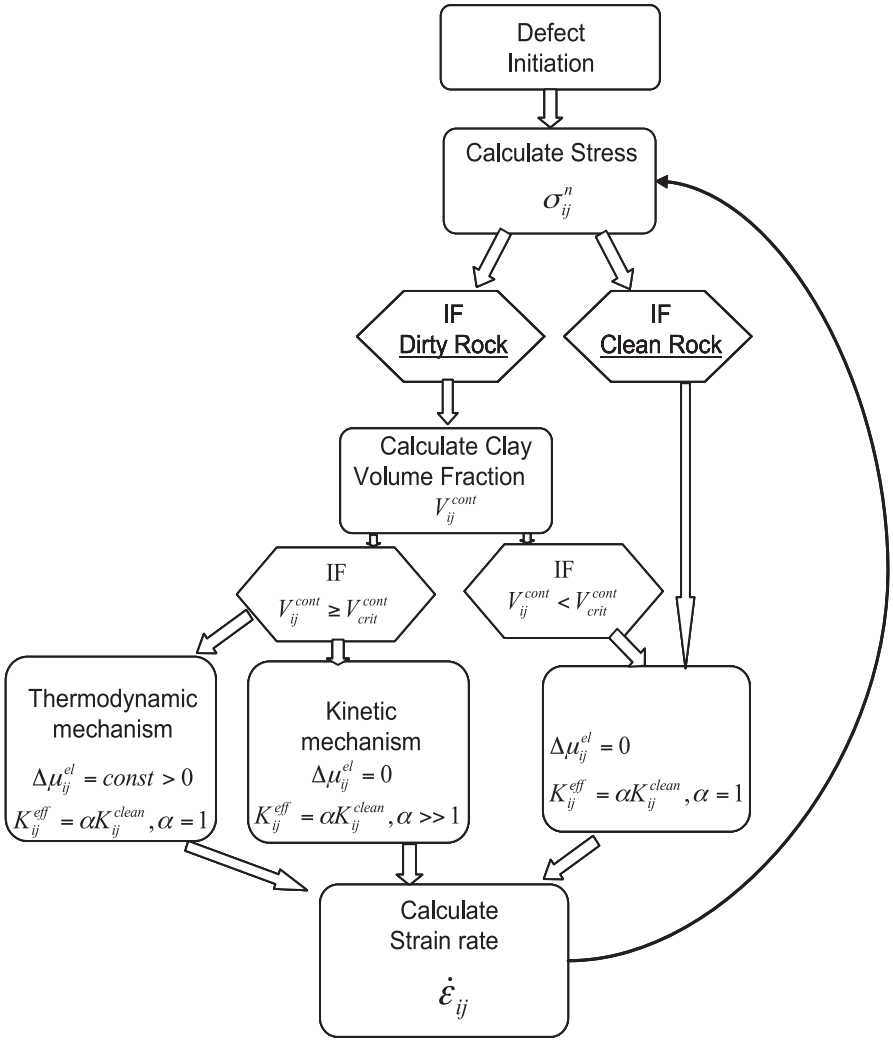

Fig. 5. A schematic description of the modeling procedure.

5. *Back to Step I:* based on the new distance between the grain centers after compaction, $l_{ij}^{eq}(t)$ (figs. 2, 3), the new stress, σ_{ij}^{n}, and the new local clay volume fraction within grain contacts, V_{ij}^{cont}, are recalculated.

SIMULATION CONDITIONS

A 50×150 lattice is utilized (fig. 3A) representing a hexagonal packing of spherical grains with diameter $l_0^{eq} = 0.5mm$, and a Young's modulus of $E = 19GPa$. Before the simulation onset grains are truncated at their contacts, in order to form grain contacts of finite size (initial contact radius $a_0 = 0.1mm$), with initial truncated distance between grain centers $l^{eq} = 0.455mm$. Constant stress boundary conditions with $\sigma_L \cong 100MPa$ are applied to the upper and lower lattice boundaries (fig. 3A), whereas the other two boundaries remain free. Simulations are initiated with a seed defect (fig. 6) 30 units long (equivalent to ~1.5 cm), in which grains have undergone

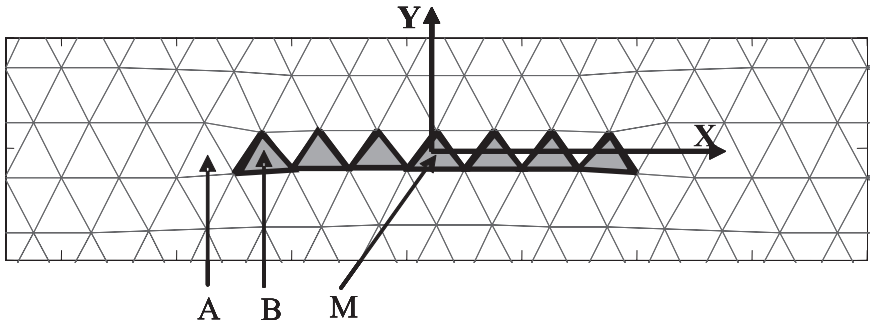

Fig. 6. A schematic representation of a dissolved defect (gray triangles), as it appears in our hexagonal spring network model, and representation of regions within and around the defect: material outside the defect tip (unit A); material inside the defect tip (unit B). The letter M defines the defect's middle.

an initial dissolution of *1 percent* ($5\mu m$). The modeling presented here simulates quartz dissolution, with parameters given in table 1. Two types of simulations, "dirty" and "clean", are run, referring to rocks initiated with and without clay respectively. The dirty rocks have an initial insoluble volume fraction of clays at each unit of the lattice, $V_0 = 1.5$ *percent*. The critical volume fraction of clays within the contact, V_{crit}^{cont}, is derived from the porosity-depth trends for different clays in figure 9 of Mondol and others (2007). At a depth of *5km* and an effective stress of *100MPa*, the reported porosity of different clays ranges from *10 percent* to *45 percent*, which corresponds to a clay volume fraction ranging from *90 percent* to *55 percent*. Thus, the critical volume fraction of clays within the contact V_{crit}^{cont} is set here to *0.8*, equivalent to *80 percent* of the contact volume occupied by clays (see Appendix). The value of K^{eff} in the presence of such a clay coating is taken to range between *2* and *100* times larger than in clean rocks, that is $\alpha =$ 2–100 (Hickman and Evans, 1995; Rutter and Wanten, 2000; Renard and others, 2001). The value for $\Delta\mu^{el}$ is not constrained by experiments, but the recent experiments of Greene and others (2009) indicate it is as large as the stress driving force. Thus we choose $\Delta\mu^{el}$ equal to, or larger than, the maximum value of the stress driven chemical potential in the initial system $\Delta\mu^{ch} = (\sigma^n - P)/\rho^s$ (this maximum value is obtained at the defect tip unit A, fig. 6).

Four sets of simulations are performed. The first two are run in order to isolate the affects of the two major mechanisms discussed—clay and stress, while the last two sets investigate the combined effect of the two mechanisms:

i. Dissolution driven only by stress (in a clean rock);
ii. Dissolution driven by clays only, via an electric potential increase, $\Delta\mu^{el}$ (dirty rock with Thermodynamic mechanism, above), with no stress affect;
iii. Dissolution driven by stresses, where clays enhance reaction rate, K^{eff} (dirty rock with Kinetic mechanism, above);
iv. Dissolution driven by stresses and clays, acting via a combined electrochemical potential increase, $\Delta\mu^{g}$ (dirty rock with Thermodynamic mechanism, above).

Figures 7–10, show the stress in a cross-section along the defect, (normalized to the far-field stress), the dissolution rate along the defect (*m/s*), and the cumulative dissolution *W(m)*. Pore pressure *P* (eq 7) is chosen equal to zero to avoid undesirable affects of choosing a specific value for *P*. This choice promotes overall dissolution in the system including contacts far from the defect, and therefore create a "background dissolution" that may be subtracted at any instance. Time indicated in the legend is in years.

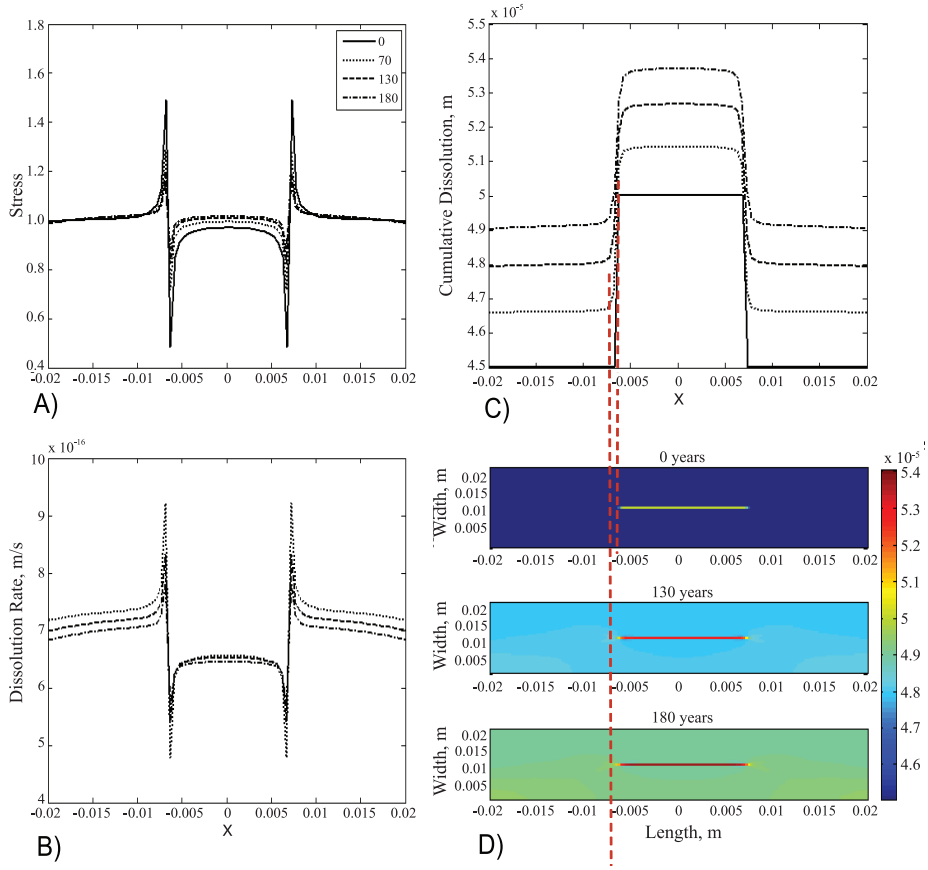

Fig. 7. Simulation set I: Dissolution driven by stress only, starting with a 'seed' defect (placed at t=0 between x=−7*mm* and x=7*mm*), that has undergone 1% dissolution, as in figure 6. The different lines represent results obtained after running the model for different times (in years). Stresses are normalized to the applied stress; dissolution rate is in *m/s*, while cumulative dissolution is in *m*. (A) Stress along the defect: The initial compressive stress peaks cause local dissolution at the tip, leading to diminished stress concentration with time. (B) Dissolution rate: Dissolution is highest at the compressive stress peaks. The dissolution rate subsides with time, following the subsiding stress at the tip. Due to the low stress on the defect flanks (see panel a) only a small amount of PS occurs on the defect flanks and away from the tip. (C) Cumulative dissolution along the defect: Flank dissolution is approximately equal to the background dissolution in the matrix. The cumulative amount of the dissolution indicates that the defect basically stops propagating sideways. (D) 2-D snapshots of cumulative dissolution indicate that dissolution does not further localize on the defect.

RESULTS

Simulation Set I: Dissolution Driven by Stress Only

In this set, $\Delta\mu^g = \sigma^n/\rho^s$ in equation (7). This set simulates a clean rock (without clay enhanced dissolution). Figure 7(A-D) shows the temporal evolution of stress, dissolution rate, and cumulative dissolution along and around a prescribed defect. The initial stress distribution (at *t= 0 years*) is characterized by an almost uniform compressive stress along the defect (fig. 7A), and low and high stress peaks at the defect tips (units B and A respectively, fig. 6). This stress pattern around a dissolution defect is analyzed in detail, both analytically and numerically in (Katsman and others, 2006a, 2006b). The next thing seen in the model is that the spiky stress pattern induces an

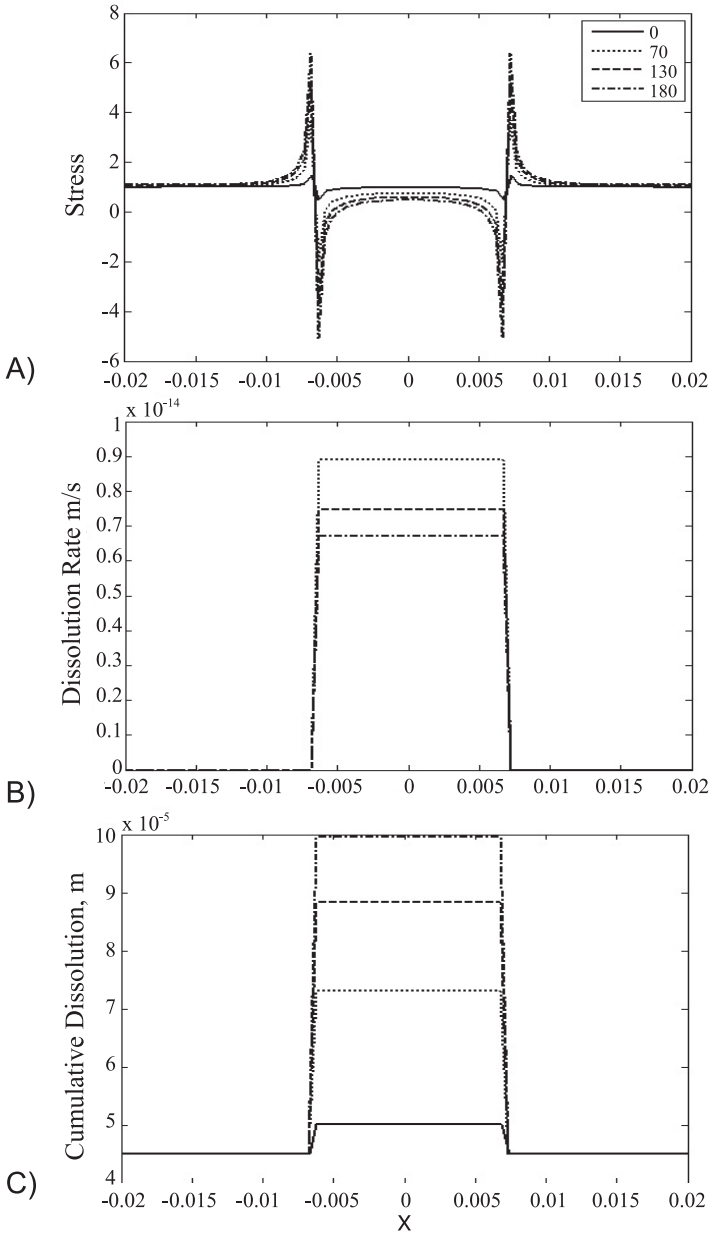

Fig. 8. Simulation set II: Dissolution driven by clays only (with no stress affect), via electric potential increase. Simulations start with a 'seed' defect that has undergone 1% dissolution, as in figure 6. Units as in figure 7. Due to the initial dissolution, the defect has accumulated a continuous layer of clays, and so experiences clay-enhanced dissolution there. (A) Stress along the defect: Stress pattern does not change significantly, though the stress peaks at the defect tip grow slowly due to the increasing amount of the dissolved matter within the defect. (B) Dissolution rate and (C) Cumulative dissolution along the defect: Dissolution is concentrated only at the defect's flanks, where clays initially accumulated. Thus dissolution thickens the initial defect, but does not lengthen it, since PS is not allowed in this set and there is not enough clays outside the defect ($V^{cont} < V^{cont}_{crit}$) to cause clay-enhanced dissolution there.

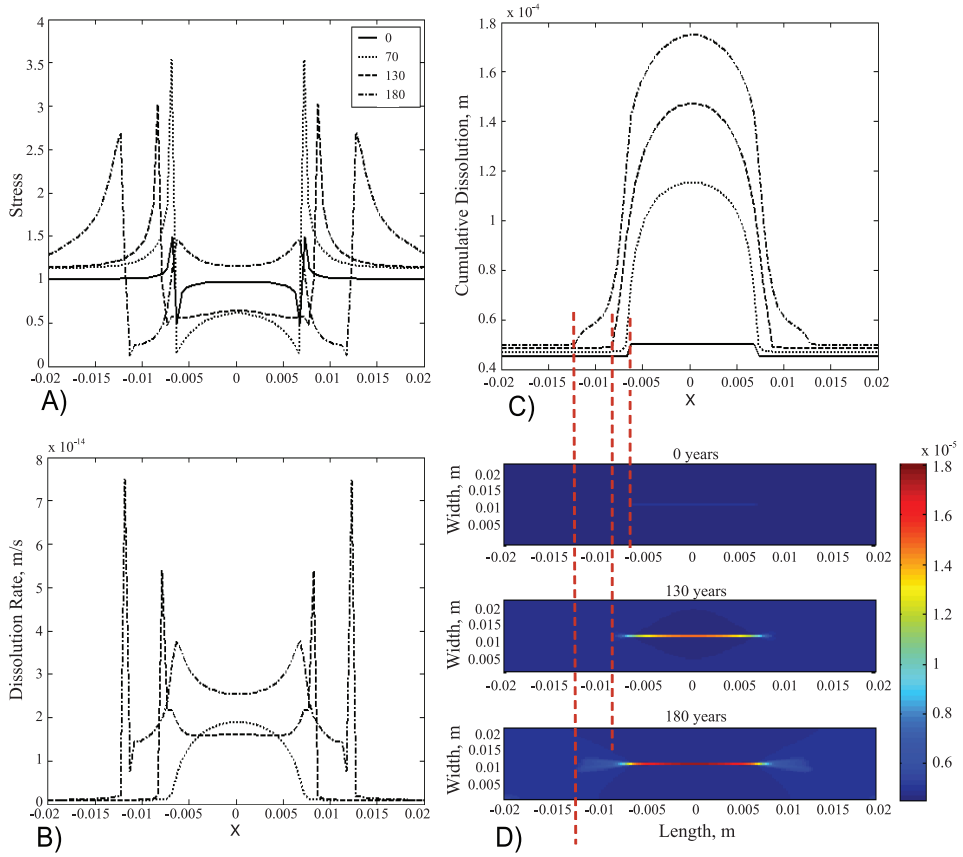

Fig. 9. Simulation set III: dissolution driven by stresses, where clays *enhance Reaction rate constant, K^{eff}, by a 100 fold.* Simulations start with a 'seed' defect that has undergone 1% dissolution, as in figure 7. Due to the initial dissolution, the defect has accumulated a continuous layer of clays, and so experiences clay-enhanced dissolution there. Units are also as in figure 7. (A) Stress along the defect: As a result of mainly clay-induced dissolution within the defect, the stress peaks outside the defect tips slowly grow, enhancing stress-driven dissolution there. Once V^{cont} at the tip exceeds V^{cont}_{crit}, *Reaction rate constant, K^{eff}, increases by a 100 fold.* Rapid tip dissolution is self-limiting: the rapid removal of material by dissolution decreases the stress peak at the tip and a new stress peak grows at the adjacent unit. (B) Dissolution rate: Dissolution is highest at the tips, leading to lateral migration of the defect tip. However some dissolution occurs along the defect leading to its thickening. (C) Cumulative dissolution along the defect: At the same time that the defect lengthens due to stress-induced dissolution, it continues to thicken due to the clays within it (the stresses are quite low there, so they don't provide enough driving force for dissolution). (D) 2D snapshots of cumulative dissolution indicate that dissolution proceeds laterally, creating a small process zone at the tip.

equally spiky dissolution pattern: The large compressive stress outside the defect tip causes local dissolution at the tips. Due to removal of material at the tip, the stress peak is smeared and reduced with time (fig. 7A). Since the dissolution rate (fig. 7B) follows the stress pattern, the dissolution rate is also smeared and subsides with time. Moreover, only a small amount of dissolution occurs along the defect flanks (that is, small amount of thickening of the defect), as stress on the flank is quite low (fig. 7B). Flank dissolution is approximately equal to background dissolution in the matrix. The cumulative amount of the dissolution (fig. 7C) and the movie snapshots of stylolite propagation (fig. 7D) indicate that dissolution does not further localize onto the defect, and after a short time the defect stops propagating.

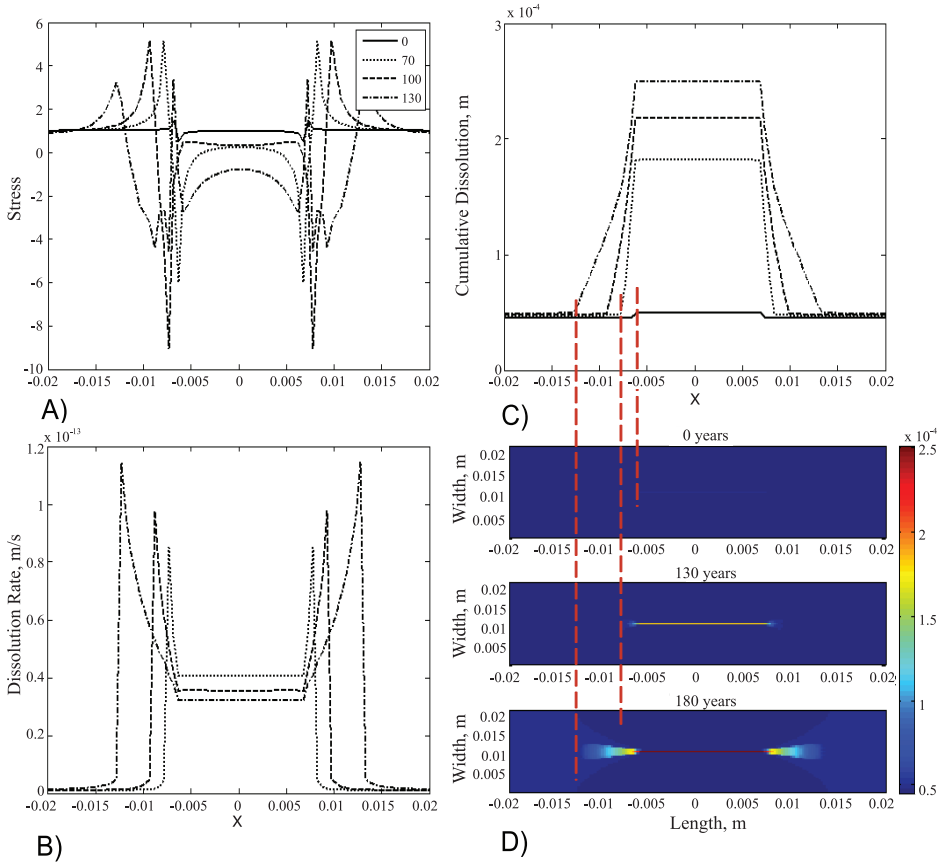

Fig. 10. Simulation set IV: dissolution driven by both stresses and clays, acting *via a combined electrochemical potential increase* with $\Delta\mu^{el} \cong 10\Delta\mu^{ch}$ at the defect tip. Simulations start with a 'seed' defect that has undergone 1% dissolution, as in figure 6. Due to the initial dissolution, the defect has accumulated a continuous layer of clays, and so experiences clay-enhanced dissolution there. Symbols and units follow figure 7. (A) Stress along the defect: As a result of mainly clay-induced dissolution within the defect, the stress peaks outside the defect tips slowly grow, enhancing stress-driven dissolution there. Once V^{cont} at the tip exceeds V^{cont}_{crit}, an electrical potential difference is established, $\Delta\mu^{el} = const > 0$ significantly increasing the total driving force for dissolution $\Delta\mu^{g}$. Rapid dissolution at the peak decreases the stress peak and a new stress peak grows at the adjacent unit. (B) Dissolution rate: Dissolution is highest at the tips, leading to lateral migration of the defect tip. (C) Cumulative dissolution along the defect: At the same time that the defect lengthens due to stress-induced dissolution, it continues to thicken due to the clays within it (the stresses are quite low there, so they don't provide enough driving force for dissolution). (D) 2D snapshots of cumulative dissolution indicate that dissolution proceeds laterally, creating a small process zone at the tip.

Simulation Set II: Dissolution Driven by Clays Only (With No Stress Affect), Via Electric Potential Increase

In this set we investigate a hypothetical dirty rock where there are *no* pressure affects on the dissolution, and only consider the differences in electric potential due to variations in clay concentrations, so that $\Delta\mu^{g} = \Delta\mu^{el}$ in equation (7). Results are presented in figure 8(A-C).

The simulations are initiated with a uniform clay distribution, V_0. The initial stress pattern (fig. 8A) is the same as in Set I. Results show that dissolution in this case concentrates only on the defect's flanks (figs. 8B and 8C), where a large amount of clay ($V^{cont} \geq V^{cont}_{crit}$) has initially accumulated due to the prescribed initial dissolution.

Dissolution on the defect flanks thickens (that is, continues to dissolve) the initial defect, but does not lengthen it (fig. 8C). The stress peaks outside the defect grow slowly due to the growing amount of the dissolved matter within the defect, figure 8A (Katsman and others, 2006a, 2006b). However, since stress plays no role in this set of simulations, the defect does not elongate. Though the driving potential ($\Delta\mu^g = \Delta\mu^{el}$) remains constant with time on the defect flanks, the dissolution rate on the flanks decreases with time (fig. 8B) since the rate constant, K^{eff}, depends strongly on the growing contact radius, a ($\sim a^{-2}$, eq 2). All in all, dissolution proceeds on the defect's flanks only, thickening the initial stylolite with time, but no lateral stylolite propagation occurs.

Simulation Set III: Dissolution Driven by Stresses in a Dirty Rock, Where Clays Enhance the Reaction Rate, K^{eff}

We tested the affects of four α values (see *Kinetic Mechanism* section), with α =2, 5, 10, and 100. In this set, as in Set I, $\Delta\mu^g = \sigma^n/\rho^s$ in equation (7). However, in contrast to Set I, this set is also initiated with a volume fraction of insoluble clays, V_0 (similarly to Set II). Results of simulations with $\alpha = 100$ are presented in figure 9. Already the small amount of initial dissolution within the defect increases clay volume fraction within it, leading to enhanced effective reaction rates there (fig. 4A). An increase of effective rate by more than a ten-fold, that is $\alpha > 10$, is sufficient to offset the relatively low driving force for the dissolution caused by the low stress on the flanks (fig. 9A), producing a net amplification of dissolution within the defect.

At the tips outside the defect (unit A, fig. 6) where the stress peaks, the driving force for dissolution is the largest (fig. 9B). Continued dissolution there slowly reduces the stress, but at the same time, accumulates clay (that is increases V^{cont}). Finally, when $V^{cont} \geq V^{cont}_{crit}$, clays enhance the effective rate constant at the tips, so that α jumps from 1 to $\alpha \gg 1$. Once this occurs, the dissolution rate at the tips increases due to both the still enhanced stresses at the tips and the presence of clays. However, rapid tip dissolution is self-limiting: the rapid removal of material by dissolution (although resulting in increased clay content) diminishes the stress peak (fig. 9A). As the stress peak decreases, a new stress peak at the adjacent unit, where the dissolution is small, grows. The process thus leads to lateral propagation of the defect tip. The dissolution rate is depicted in figure 9B, where it is seen that dissolution is mostly concentrated at the migrating stress peaks. At the same time that the defect lengthens, it continues to thicken due to the clay enhanced dissolution rates within it (figs. 9 C-D). This is the main mechanism of the combined clay-stress-induced dissolution, when clays drive dissolution via an elevated reaction rate. In summary, the stress peaks outside the defect tips (unit A) drive stylolite elongation, while clays within the defect drive stylolite thickening. Only if clay-enhanced rates are large enough to compensate for the reduced stresses and thus the resulting low drive for dissolution (that is $\alpha \gg 1$), does the defect propagate. We find numerically that enhancement of K^{eff} by clays must be at least 10 fold ($\alpha \geq 10$) in order for the defect to propagate.

Simulation Set IV: Dissolution Driven by Both Stresses and Clays in a Dirty Rock, Acting Via a Combined Electrochemical Potential Increase

Here $\Delta\mu^g = \sigma^n/\rho^s + \Delta\mu^{el}$ in equation (7), where clays act to increase the electrochemical potential difference along grain boundaries, as in equations (8). A set of simulations with $\Delta\mu^{el} \cong 10\Delta\mu^{ch}$ at the tip is presented in figure 10.

Again, simulations are initiated with a uniform clay distribution, V_0. Following the introduction of a seed dissolution defect, a large amount of insoluble clay, $V^{cont} \geq V^{cont}_{crit}$, concentrates within the defect, as in *Simulation Sets II and III*. At this stage, clay-enhanced dissolution takes place only within the initial defect (on the flanks), and is driven by the elevated electrochemical potential in the presence of clays. Since stress is

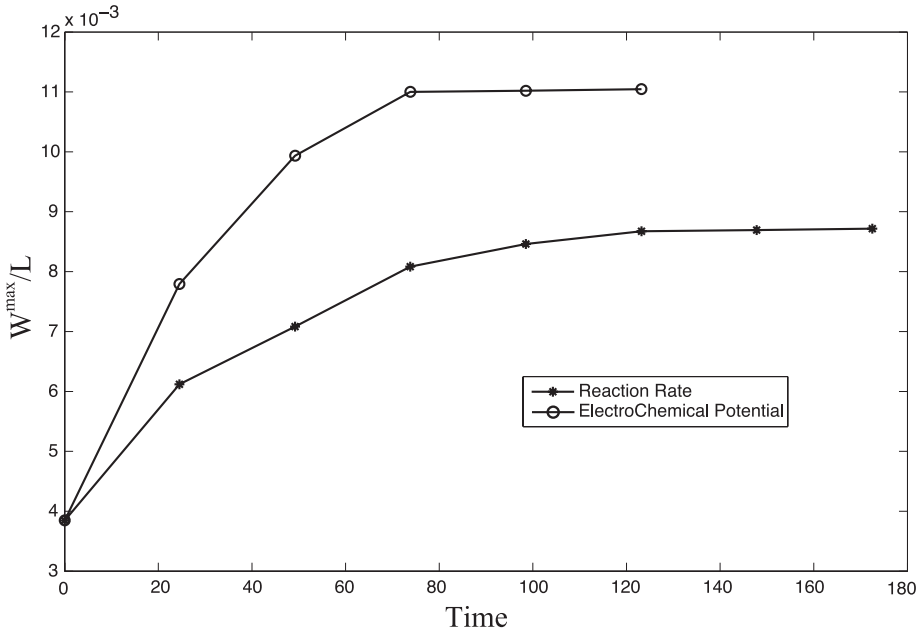

Fig. 11. The ratio of maximal dissolution within the stylolite (unit M, fig. 6) to the stylolite length (W^{max}/L), versus time. Modeled stylolites start demonstrating self-similar profiles after about 120 years when clays act via Reaction Rate increase and after about 75 years when clays act via Electrochemical potential introduction. Saturation value is about 0.0086 in the former case and 0.011 in the later case.

quite low within the defect (fig. 10A), very little stress-induced dissolution occurs there. As a result of mainly clay-induced dissolution within the defect, the stress peaks outside the defect tips slowly grow, enhancing stress-driven dissolution there (unit A, fig. 6). As dissolution proceeds, the volume fraction V of clays at the tips increases. Once $V^{cont} \geq V^{cont}_{crit}$ (fig. 4B), an electrical potential difference is established, $\Delta\mu^{el} = const > 0$, significantly increasing the total driving force for dissolution $\Delta\mu^{g}$ at the defect tip (unit A, fig. 6). Thus, the dissolution rate at the tip is enhanced due to both the enhanced stresses there and the established electric potential difference caused by the accumulation of clays. As explained above, rapid tip dissolution is self-limiting: the rapid removal of material by dissolution diminishes the stress peak (fig. 10A). As the stress peak at point A diminishes, a new stress peak grows at the adjacent unit. This process leads to lateral migration of the defect tip. The dissolution rate is depicted in figure 10B, showing that dissolution is mostly concentrated at the migrating stress peaks. At the same time that the defect lengthens, it continues to thicken due to the clays within it (the stresses are quite low there, so they don't provide much driving force for dissolution), as depicted in figures 10(C-D). This is the main mechanism of the combined clay-stress-induced dissolution: the stress peaks outside the defect tips (unit A, fig. 6) drive stylolite elongation, while clays within the defect drive stylolite thickening.

Figure 11 shows the ratio of maximal dissolution within the stylolite (unit M, fig. 6) to the stylolite length (W^{max}/L), versus time. Modeled stylolites start demonstrating self-similar profiles after about 120 years when clays act via Reaction Rate increase (in case of $\alpha = 100$) and after about 75 years when clays act via Electrochemical potential introduction. The resulting self-similar profile means that stylolites lengthen in propor-

tion to the amount that they thicken, with the ratio saturating at about 0.0086 in the former case and 0.011 in the later case.

DISCUSSION

The simulations presented in this paper systematically investigate the mechanism and feasibility of spontaneous localization of chemical compaction. For this purpose, a new numerical model was developed, a variant of an SNM model that was used in previous works to successfully explain mechanical compaction bands formation and propagation (Katsman and others, 2005; Katsman and Aharonov, 2006). This new numerical technique allows modeling the dynamic evolution of irreversible strain driven by chemical compaction, and the resulting dynamic elastic stress field. In particular our model allows investigation of the anti-crack hypothesis for localizing PS from an initially uniformly distributed (that is intergranular) pressure solution. The anticrack hypothesis (Fletcher and Pollard, 1981) suggested a feedback between pressure solution driven strain and the stress field to explain stylolite propagation and growth. This hypothesis postulated that a localized pressure solution defect produces a compressive stress concentration at its tips, which in turn leads to further PS at the tips and thus elongation of the defect. The anti-crack hypothesis further postulated that PS is also enhanced on stylolite flanks, due to high stresses that are presumed to develop there, so that stylolites will thicken by PS as they lengthen and retain a self-similar shape, similar to cracks.

Our simulations however do not find that PS spontaneously localizes into self-propagating dissolution defects. We are also unaware of other works that model stylolite growth via this process (without adding clays). In order for defects to spontaneously propagate we find that another dissolution catalyst, in addition to stress, is needed. Specifically the catalyzing effect of residual clays (which was suggested in scores of works) is found to be the perfect missing ingredient to induce PS localization.

Simulation Set I tested the feasibility of the anticrack hypothesis (Fletcher and Pollard, 1981), by introducing normal stress as the single driving force for dissolution. The results of this set suggest that PS alone does not produce propagating and growing stylolites. The reason is that, as calculated by Katsman and others (2006a, 2006b), a defect from which volume is removed does not produce an (anti)crack-like stress field. Instead, such a volume reduction defect may be described as an Eshelby inclusion (Eshelby, 1957) (transformation problem) or, alternatively, as an edge dislocation. The source of the stress enhancement at the volume reduction defect tips is a geometrical incompatibility due to the localized volume removal from the surrounding matrix, rather than stiffness loss as in cracks. The stress concentrations at the tips of such defects are different than in cracks. Maybe the most important difference from the anticrack hypothesis is that stress is calculated to be low on the defect flanks. This analysis led Katsman and others (2006a, 2006b) to predict that stress-induced dissolution processes will be suppressed (rather than enhanced) on the defects flanks. This prediction agrees with Simulation Set I.

Although one may postulate that PS defects will propagate laterally via a process similar to growth of mechanical compaction bands (Katsman and others, 2005; Katsman and Aharonov, 2006), the PS defects in Set I do not lengthen with time (fig. 7). Instead, the lateral defect propagation stops shortly after the simulation onset. This difference may be explained as follows: The compressive stress at the dissolution defect tip is dominated by the volume of matter removed near the tip, that is by the irreversible strain due to dissolution, and its gradient within the defect near the tip (Katsman and others, 2006a, 2006b). Pressure solution is different from mechanical compaction: Pressure solution occurs without a 'stress threshold', and the stress-induced dissolution process at the tip of a stylolite is gradual. Hence, the geometry of a stylolite tip is progressively 'smeared', diffusing the stress and limiting the process.

Lateral defect propagation requires an additional mechanism that will continue dissolution on the stylolite flanks, that is continue to remove more matter close to the tip, and by this maintain a high stress at the tip (as in Simulation Set II). We propose that this mechanism is provided by clay enhancement of dissolution.

Strong evidence points to the important role of clays in producing chemical compaction in general (Heald, 1956; Marshak and Engelder, 1985; Ehrenberg, 1990; Bjørkum, 1996; Oelkers and others, 1996; Greene and others, 2009), and in localizing stylolites in particular (Walderhaug, 2004, 2006). We added clay affects to our model by accumulating clays at grain contacts (from an initially diffuse distribution) in Simulations II–IV. Since the process by which clays enhance dissolution is unclear, we tested in our model the two commonly suggested processes by which accumulated clays may significantly alter the behavior at the grains' contacts: the first is by changing diffusion rates and the second is by altering electro-chemical potential.

The first of the two possible clay affects is tested in *Simulation Set III*. Dissolution is driven by stress alone, while clay coating at the grain-contact enhances diffusion rates and by that, enhances reaction rates (for example Renard and others, 1997, 2001). This set shows both stylolite elongation and thickening. The overall stylolite propagation mechanism can be explained as follows. The defect is lined with clays, enhancing dissolution on the flanks. On the other hand, dissolution is driven by stress at the defect tip, where compressive stress is high and still no clays affect dissolution. As PS progresses at the tip, the stress drops there, but at the same time clays accumulate, switching with time from PS at this location to clay-enhanced dissolution, and the tip moves outwards. This mechanism allows a propagating self-similar stylolite.

When dissolution is driven by clays only without a stress affect, as in *Simulation Set II,* clay-induced dissolution on defect flanks thickens the initial defect, but does not elongate it. When both stress and clay affects are included in a generalized electrochemical potential, as in *Simulation Set IV,* modeled stylolites both thicken and elongate with time. This mechanism also allows a propagating self-similar stylolite. Mardon (ms, 1988) found in field measurements on carbonates solution seams from the Valley and Ridge formation in Pennsylvania that the ratio of maximum thickness of dissolved matter, W_{max}, to stylolite length, L, is approximately constant, with $W_{\max}/L \cong 0.03$. Figure 11 shows the important modeling result of a developing self-similar stylolite profile, with a ratio about 3 times smaller than in the field. This ratio depends on the details of the kinetics of the clay-enhanced dissolution, which is not known. It should be noted that there are also observations of stylolites that are believed to localize on preexisting clay laminae (Walderhaug and Bjørkum, 2003; Laronne and others, manuscript in preparation) and never propagate laterally along a defect. Instead, the extent of the originally present clay lamina determined their lateral extent. In such stylolites self-similar shapes are not expected.

At this stage we wish to discuss an important field observation related to stylolites and to our modeling results. Field observations find that cement material, originating from dissolution on stylolites, precipitates in close proximity to the stylolite—right outside the seam. In the Jurassic Barents Sea sandstones, all silica dissolution is attributed to stylolites, and there are interesting cases where the cement precipitation is concentrated within a few centimeter thick band adjacent to the seam (Wangen, 1998; Walderhaug and Bjørkum, 2003). Corwin and others (1997) observe in the carbonates of the Upper Smackover formation similar narrow zones of low porosity, most likely due to massive precipitation adjacent to stylolites. These observations bring into question the role of stress as the sole controlling factor in dissolution and precipitation, since stress is a smoothly decaying hyperbolic function. If stress was high on stylolite flanks (as assumed by the anticrack model) it has to be still somewhat high in the region adjacent to the stylolite, relative to the ambient stress field. Such a

Table 2

A checklist for stylolite growth

Process	Elongation	Thickening
Dissolution driven by stress only (Set I)	No	No
Dissolution driven by clays only (with no stress affect), via electric potential increase (Set II)	No	Yes
Dissolution driven by stress, while clays enhance reaction rate (Set III)	Yes	Yes
Dissolution driven by stresses and clays, acting via a combined electrochemical potential increase (set IV)	Yes	Yes

situation would promote a zone, a few centimeters wide, of overall dissolution, instead of overall precipitation in the vicinity of stylolites, as observed. It is difficult to attribute the observed small scale spatial variations, from overall strong dissolution on the stylolites to overall strong precipitation right outside the stylolites, to stress variations alone. Very strong gradients between dissolution and precipitation are more easily explained by clay-induced dissolution at the seam (Heald, 1956). Clay induced dissolution requires actual contact between clay and mineral to enhance dissolution. Right outside the seam the absence of massive amounts of clays results in a lower chemical potential and thus precipitation. These field observations agree with our suggestion that clays or other matter accumulated within the stylolites enhance dissolution and couple to stress as equal partners in stylolite formation.

Another observation related to the field is that 2D snapshots of propagating stylolites (figs. 9D and 10D) show a dissolution process zone surrounding the defect tip. The process zone shown in the simulation is generated by the finite area of enhanced stresses around the defect tip, due to the non-local stress affects. These enhanced stresses lead to the enhanced dissolution at the region surrounding the defect tip. Similar process zones were observed around natural stylolite tips (Meike and Wenk, 1988; Raynaud and Carrio-Schaffhausser, 1992).

We note that the stylolite propagation patterns simulated in Set III (fig. 9) and Set IV (fig. 10) are similar. This similarity stems from equation (6), from which it is seen that increasing either K^{eff} or $\Delta\mu^{g}$ leads to indistinguishable dissolution patterns. Thus it is not possible at this stage to differentiate between rate enhancement and changes in driving force. A checklist for stylolite growth conditions is presented in table 2.

The current model is the first stage of our project, aiming to test the initial stages of stylolite propagation starting from a localized "seed" defect and assuming constant pore-fluid composition and almost constant porosity. It is easy to show that for the amount of dissolution considered the precipitation is negligible and model assumptions are correct.

Conclusions

This manuscript presents a systematic numerical investigation of mechanisms that may possibly be responsible for growth of dissolution defects (solution seams and stylolites). The simulations study processes by which lateral propagation and thickening of dissolution defects occurs. The roughening of the solution surfaces is not explored. The mechanisms tested for stylolite growth were thin-film PS and clay-enhanced dissolution, where two clay dissolution-enhancement mechanisms were tested: clay-enhanced reaction rate and clay-induced electrochemical potential differences.

Stress pattern analysis predicts (as discussed in Katsman and others, 2006a, 2006b) that stress-induced volume reduction (like PS or mechanical compaction) may lengthen defects but may not thicken them. In agreement with this prediction, mechanical compaction bands show no thickening with time (Klein and others, 2001; Haimson and Kovachich, 2003). In contrast, field observations indicate that stylolites are a location of continued dissolution, with often 50 percent of rock mass dissolved at their flanks. This paper suggests that PS alone cannot account for stylolite formation: the special condition that allows continued dissolution on stylolite flanks, despite the low stress there, may be their clay lining. Simulation results suggest that only when both PS and clay-enhanced dissolution operate in unison do stylolites propagate: PS operates at the defect tips to elongate the stylolite, while accumulated clays continuously dissolve matter by clay-enhanced dissolution on the stylolite flanks. This combination of processes results in a self-similar defect shape where the maximum amount of dissolution in the middle is proportional to the length of the defect, in agreement with field observations of some stylolites (Mardon, ms, 1988). The details of the shape are expected to depend on the exact details of the processes and on material heterogeneity. There is ample field evidence that clays (also possibly organic matter) play a major role in what is considered to be PS, and our results add to this evidence, suggesting that without accumulating clay lining (or a lining of some other dissolution catalyst) stylolites wouldn't localize.

To our knowledge, there are no published reports of experiments that successfully observed growing macroscopic (that is longer than a single grain) stylolites. In such a situation, numerical and analytical tools provide an important avenue to quantitatively assess suggested mechanisms for development of geological structures. Hopefully, following our conclusions indicating the importance of clays to the localization process, new experiments will be conducted a) to test the mechanism by which clays enhance PS and b) to attempt to form stylolites with the presence of clays. In this plan of combined modeling and experiments, progress may be achieved in understanding these important geological features.

ACKNOWLEDGMENTS

This research is supported by a grant from the ISF. EA was incumbent of the Anna and Maurice Boukstein Career Development Chair. We wish to thank Drs. H. Scher, E. Sass, D. Ertas, Z. Karcz, D. Polizzoti, C. Scholz, R. Fletcher, B. Evans, and Y. Eyal for helpful and interesting discussions. We thank L. Laronne for reviewing the clay literature. We thank both reviewers for their thorough reviews and helpful suggestions.

Appendix

Volume Fraction of Clays Within a Contact, V^{cont}

Points *A*, *B*, and *C* are located at grain centers (fig. 3B). Initially clay is randomly distributed within the curvilinear triangle *DEF*, which represents the pore space (fig. 3B, left figure). Before any dissolution takes place, the volume fraction of clays V_0, is defined as:

$$V_0 = \frac{S_{clays}}{S_{ABC}} \tag{A1}$$

where S_{clays} is the volume of insoluble clays, and S_{ABC} is the total volume of the rock unit (that is the volume of triangle ABC, fig. 3B, left figure). The maximum possible volume fraction of clay is when it completely fills the pore space, that is $S^{\max}_{clays} = S_{DEF}$ (fig. 3B, left figure). Under these conditions, each unit of rock contains a volume fraction of clays $V_0 = 9\%$. Our simulations are initiated with a uniformly distributed volume fraction of clays, $V_0 = 1.5\%$ (to agree with Walderhaug and others, 2006). As a result, the initial volume of clays S_{clays} ($t = 0$) can be calculated from equation (A1).

After some dissolution, the equilibrium length of the diagonal springs (l^{eq}) shortens, and the contact radius, a, grows (see also fig. 2). Using the fact that $\frac{l_0^{eq}}{2} = DC$ (figs. 2, 3B, left figure), $\frac{l^{eq}}{2} = OC$ (figs. 3B, right figure), and $a = OD$ (fig. 3B, right figure) at any stage of the dissolution, clays that were initially located in the curvilinear triangle *DEF* (fig. 3B, left figure), partially accumulate in the two rectangles *GD* and *EH* and within the curvilinear triangle *DEF* that is now reduced in size (fig. 3B, right figure). We then track the clay coverage at the grain contacts. From geometrical considerations, the area of the curvilinear triangle *DEF* (fig. 3B, right figure) can be calculated at any stage of the dissolution. The clay volume, S_{clays} ($t = 0$), in *DEF* prior to dissolution (fig. 3B, left figure), is used to calculate the volume of clays, $S_{clays}(t)$, in *DEF* after dissolution (fig. 3B, right figure); and finally the volume of clays accumulated in *GD* and *EH* after dissolution, S_{clays}^{accum}, is calculated as

$$S_{clays}^{accum} = S_{clays}(t = 0) - S_{clays}(t) \tag{A2}$$

The volumes of rectangles *GD* and *EH* are $2a \times \delta$, where $a = \sqrt{(l_0^{eq})^2 - (l^{eq})^2}$ at any stage of the dissolution. Here δ is the contact thickness, taken as $\delta = 6.8\mu m$, and $\delta > \delta_0$ due to the clays trapped at the interface between the dissolving grains (fig. 3B). As a result, dividing S_{clays}^{accum} by $a \times \delta$, will provide the (non-dimensional) volume fraction of clays within the contact as:

$$V_{cont} = S_{clays}^{accum} / a\delta \tag{A3}$$

References

Aharonov, E., and Sparks D., 1999, Rigidity Phase Transition in Granular Packings: Physical Review E, v. 60, p. 6,890–6,896, doi:10.1103/PhysRevE.60.6890.

Alcantar, N., Israelachvili, J., and Boles, J., 2003, Forces and ionic transport between mica surfaces: Implication for pressure solution: Geochimica et Cosmochimica Acta, v. 67, n. 7, p. 1,289–1,304, doi:10.1016/S0016-7037(02)01270-X.

Alvarez, W., Engelder, T., and Geiser, P. A., 1978, Classification of solution cleavage in pelagic limestone: Geology, v. 6, p. 263–266, doi:10.1130/0091-7613(1978)6⟨263:COSCIP⟩2.0.CO;2.

Andrews, L. M., and Railsback, L. B., 1997, Controls on stylolite development: morphologic, lithologic and temporal evidence from bedding-parallel and transverse stylolites from the U.S. Appalachians: The Journal of Geology, v. 105, p. 59–73.

Baker, P. A., Kastner, M., Byerlee, J. D., and Lockner, D. A., 1980, Pressure Solution and Hydrothermal Recrystalization of Carbonate Sediments—An Experimental Study: Marine Geology, p. 38, p. 185–203, doi:10.1016/0025-3227(80)90058-4.

Bathurst, R. G. C., 1971, Carbonate Sediments and their Diagenesis: Amsterdam, Elsevier, 640 p.

Bayly, B., 1986, A mechanism for the development of stylolites: Journal of Geology, v. 94, p. 431–435.

Bjørkum, P. A., 1996, How Important is Pressure in Causing Dissolution of Quartz in Sandstones?: Journal of Sedimentary Research, v. 66, n. 1, p. 147–154.

Corwin, L. W., Broomhall, R. W., Saidikowski, R. M., and Wooten, J. N., 1997, Stylolites impact the miscible nitrogen flood in a mature carbonate oil field: SPE International, Inc., v. 37780, p. 213–221.

Curtin, W. A., and Scher, H., 1990a, Brittle fracture in disordered materials: A spring network model: Journal of Material Resources, v. 5, n. 3, p. 535–553, doi:10.1557/JMR.1990.0535.

——— 1990b, Mechanics modeling using a spring network: Journal of Material Resources, v. 5, n. 3, p. 554–562, doi:10.1557/JMR.1990.0554.

De Boer, R. B., 1977, On the thermodynamics of pressure solution-interaction between chemical and mechanical forces: Geochimica et Cosmochimica Acta, v. 41, p. 249–256, doi:10.1016/0016-7037(77)90232-0.

De Meer, S., and Spiers, C. J., 1999, On mechanisms and kinetics of creep by intergranular pressure solution, *in* Jamtviet, B., and Meakin, P., editors, Growth, dissolution and pattern formation in geosystems: The Netherlands, Kluwer Academic Publisher, p. 345–366.

De Meer, S., Spiers, C. J., Peach, C. J., and Watanabe, T., 2002, Diffusive properties of fluid-filled grain boundaries measured electrically during active pressure solution: Earth and Planetary Science Letters, v. 200, p. 147–157, doi:10.1016/S0012-821X(02)00585-X.

Dewers, T., and Ortoleva, P., 1990, A coupled reaction/transport/mechanical model for intergranular pressure solution, stylolites, and differential compaction and cementation in clean sandstones: Geochimica et Cosmochimica Acta, v. 54, p. 1,609–1,625, doi:10.1016/0016-7037(90)90395-2.

Ebner, M., Koehn, D., Toussaint, R., and Renard, F., 2009, The influence of rock heterogeneity on the scaling properties of simulated and natural stylolites: Journal of Structural Geology, v. 31, p. 72–82, doi:10.1016/j.jsg.2008.10.004.

Ehrenberg, S. N., 1990, Relationship between diagenesis and reservoir quality in sandstones of the Garn Formation, Haltenbanken, mid-Norwegian continental shelf: AAPG Bulletin, v. 74, n. 10, p. 1,538–1,558.

——— 2006, Porosity Destruction in Carbonate Platforms: Journal of Petroleum Geology, v. 29, n. 1, p. 41–51, doi: 10.1111/j.1747-5457.2006.00041.x.

Eshelby, J. D., 1957, The determination of the elastic field of an ellipsoidal inclusion, and related problems: Proceedings of the Royal Society of London (A), Mathematical and Physical Sciences, v. 241 (1226), p. 376–396, doi:10.1098/rspa.1957.0133.

Fletcher, R. C., and Pollard, D. D., 1981, Anticrack model for pressure solution surfaces: Geology, v. 9, p. 419–424, doi:10.1130/0091-7613(1981)9⟨419:AMFPSS⟩2.0.CO;2.

Fueten, F., and Robin, P.-Y. F., 1992, Finite element modelling of the propagation of a pressure solution cleavage seam: Journal of Structural Geology, v. 14, n. 8/9, p. 953–962, doi:10.1016/0191-8141(92)90026-S.

Fueten, F., Robin, P.-Y. F., and Schweinberger, M., 2002, Finite element modelling of the evolution of pressure solution cleavage: Journal of Structural Geology, v. 24, n. 6–7, p. 1,055–1,064, doi:10.1016/S0191-8141(01)00091-8.

Gratier, J. P., Muquet, L., Hassani, R., and Renard, F., 2005, Experimental Microstylolites in Quartz and Modeled Application to Natural Stylolitic Structures: Journal of Structural Geology, v. 27, p. 89–100, doi:10.1016/j.jsg.2004.05.007.

Greene, G. W., Kristiansen, K., Meyer, E. E., Boles, J. R., and Israelachvili, J. N., 2009, Role of Electrochemical Reactions in Pressure Solution: Geochimica et Cosmochimica Acta, v. 73, p. 2,862–2,874, doi:10.1016/j.gca.2009.02.012.

Gruzman, Y., ms, 1997, Origin of Sedimentary Stylolites from Israel: Jerusalem, Hebrew University, Institute of Earth Science, Ph. D. thesis.

Haimson, B., and Kovachich, J., 2003, Borehole instability in high-porosity Berea sandstone and factors affecting dimensions and shape of fracture-like breakouts: Engineering Geology, v. 69, p. 219–231, doi:10.1016/S0013-7952(02)00283-1.

Heald, M. T., 1956, Cementation of Simpson and St. Peter Sandstones in Parts of Oklahoma, Arkansas, and Missouri: Journal of Geology, v. 64, p. 16–30.

Hickman, S. H., and Evans, B., 1991, Experimental Pressure Solution in Halite: the Effect of Grain/Interphase Boundary Structure: Journal of the Geophysical Society, London, v. 148, p. 549–560, doi:10.1144/gsjgs.148.3.0549.

——— 1995, Kinetics of Pressure Solution at Halite-Silica Interfaces and Intergranular Clay Films: Journal of Geophysical Research, v. 100, B7, p. 13,113–13,132, doi:10.1029/95JB00911.

Karcz, Z., Aharonov, E., Ertas, D., Polizzotti, R., and Scholz, C. H., 2006, Stability of a Sodium Chloride Indenter Contact undergoing Pressure Solution: Geology, v. 34, n. 1, p. 61–63, doi:10.1130/G21722.1.

Katsman, R., and Aharonov, E., 2006, A Study of Compaction Bands Originating from Cracks, Notches, and Compacted Defects: Journal of Structural Geology, v. 28, p. 508–518, doi:10.1016/j.jsg.2005.12.007.

Katsman, R., Aharonov, E., and Scher, H., 2005, Numerical Simulation of Compaction Bands in High-Porosity Sedimentary Rocks: Mechanics of Materials, v. 37, n. 1, p. 143–162, doi:10.1016/j.mechmat.2004.01.004.

Katsman, R., Aharonov, E., and Scher, H., 2006a, A Numerical Study on Localized Volume Reduction in Elastic Media: Some Insights on the Mechanics of Anticracks: Journal of Geophysical Research, v. 111, B03204, doi: 10.1029/2004JB003607.

——— 2006b, Localized Compaction in Rocks: Eshelby's Inclusion and the Spring Network Model: Geophysical Research Letters, v. 33, L10311, doi: 10.1029/2005GL025628.

Klein, E., Baud, P., Reuschle, T., and Wong, T-F., 2001, Mechanical behavior and failure mode of Bentheim sandstone under triaxial compression: Physics and Chemistry of the Earth (A), v. 26, n. 1–2, p. 21–25, doi:10.1016/S1464-1895(01)00017-5.

Koehn, D., Renard, F., Toussaint, R., and Passchier, C. W., 2007, Growth of stylolite teeth patterns depending on normal stress and finite compaction: Earth and Planetary Science Letters, v. 257, p. 582–595, doi:10.1016/j.epsl.2007.03.015.

Lehner, F. K., 1995, A model for intergranular pressure solution in open system: Tectonophysics, v. 245, p. 153–170, doi:10.1016/0040-1951(94)00232-X.

Mardon, D., ms, 1988, Localized pressure solution and the formation of descrete solution seams: College Station, Texas, Texas A&M University, Ph. D. thesis, 246 p.

Marshak, S., and Engelder, T., 1985, Development of cleavage in limestones of a fold-thrust belt in eastern New York: Journal of Structural Geology, v. 7, n. 3/4, p. 345–359, doi:10.1016/0191-8141(85)90040-9.

Meike, A., and Wenk, H.-R., 1988, A TEM study of microstructures associated with solution cleavage in limestone: Tectonophysics, v. 154, p. 137–148, doi:10.1016/0040-1951(88)90231-4.

Merino, E., Ortoleva, P., and Strickholm, P., 1983, Generation of evenly-spaced pressure-solution seams during (late) diagenesis: A kinetic theory: Contributions to Mineralogy and Petrology, v. 82, p. 360–370, doi:10.1007/BF00399713.

Meyer, E. E., Greene, G. W., Alcantar, N. A., Israelachvili, J. N., and Boles, J. R., 2006, Experimental investigation of the dissolution of quartz by a muscovite mica surface: Implications for pressure solution: Journal of Geophysical Reasearch, v. 111, B08202, doi:10.1029/2005JB004010.

Mondol, N. H., Bjørlykke, K., Jahren, J., and Høeg, K., 2007, Experimental mechanical compaction of clay mineral aggregates—Changes in physical properties of mudstones during burial: Marine and Petroleum Geology, v. 24, p. 289–311, doi:10.1016/j.marpetgeo.2007.03.006.

Oelkers, E. H., Bjørkum, P. A., and Murphy, W. M., 1996, A Petrographic and Computational Investigation of Quartz Cementation and Porosity Reduction in North Sea Sandstones: American Journal of Science, v. 296, p. 420–452.

Oldershaw, A. E., and Scoffin, T. P., 1967, The source of ferroan and non-ferroan calcite cements in the Halkin and Wenlock limestones: Geological Journal, v. 5, p. 309–320.

Paterson, M. S., 1973, Nonhydrostatic thermodynamics and its geologic applications: Reviews of Geophysics, v. 11, n. 2, p. 355–389, doi:10.1029/RG011i002p00355.

——— 1995, A theory for granular flow accommodated by material transfer via an intergranular fluid: Tectonophysics, v. 245, n. 3–4, p. 135–151,[00ff]20doi:10.1016/0040-1951(94)00231-W.
Radjai, F., Wolf, D. E., Jean, M., and Moreau, J. J., 1998, Bimodal character of stress transmission in granular packings: Physical Review Letters, v. 80, n. 1, p. 61–64, doi:10.1103/PhysRevLett.80.61.
Railsback, L. B., 1993, Lithologic controls on morphology of pressure-dissolution surfaces (stylolites and dissolution seams) in Paleozoic carbonate rocks from the mideastern United States: Journal of Sedimentary Petrology, v. 63, p. 513–522.
——— 1998, Evaluation of spacing of stylolites and its implication for self-organization of pressure dissolution: Journal of Sedimentary Research, v. 68, n. 1, p. 2–7.
Raynaud, S., and Carrio-Schaffhausser, E., 1992, Rock matrix structure in a zone influenced by a stylolite: Journal of Structural Geology, v. 14, p. 973–980, doi:10.1016/0191-8141(92)90028-U.
Renard, F., Ortoleva, P., and Gratier, J. P., 1997, Pressure solution in sandstones: influence of clays and dependence on temperature and stress: Tectonophysics, v. 280, p. 257–266, doi:10.1016/S0040-1951(97)00039-5.
Renard, F., Dysthe, D., Feder, J., Bjorlykke, K., and Jamtveit, B., 2001, Enhanced pressure solution creep rates induced by clay particles: Experimental evidence in salt aggregates: Geophysical Research Letters, v. 28, n. 7, p. 1,295–1,298.
Rutter, E. H., and Elliott, D., 1976, The Kinetics of Rock Deformation by Pressure Solution [and Discussion]: Philosophical Transactions of the Royal Society of London series A, v. 283, p. 203–219, doi: 10.1098/rsta.1976.0079.
Rutter, E. H., and Wanten, P. H., 2000, Experimental Study of the Compaction of Phyllosilicate-Bearing Sand at Elevated Temperature and with Controlled Pore Water Pressure: Journal of Sedimentary Research, v. 70, n. 1, p. 107–116, doi:10.1306/2DC40902-0E47-11D7-8643000102C1865D.
Safaricz, M., and Davison, I., 2005, Pressure solution in chalk: AAPG Bulletin, v. 89, p. 383–401, doi:10.1306/10250404015.
Sheldon, H. A., Wheeler, J., Worden, R. H., and Cheadle, M. J., 2003, An Analysis of the Role of Stress, Temperature, and pH in Chemical Compaction of Sandstones: Journal of Sedimentary Research, v. 73, n. 1, p. 64–71, doi: 10.1306/070802730064.
Shimizu, I., 1995, Kinetics of pressure solution creep in quartz: theoretical considerations: Tectonophysics, v. 245, p. 121–134, doi:10.1016/0040-1951(94)00230-7.
Sibley, D. F., and Blatt, H., 1976, Intergranular Pressure Solution and Cementation of the Tuscarora Orthoquartzite: Journal of Sedimentary Petrology, v. 46, n. 4, p. 881–896.
Stockdale, P. B., 1922, Stylolites: Their Nature and Origin: Indiana University Studies, v. 9, p. 1–97.
Tada, R., and Siever, R., 1989, Pressure solution during diagenesis: Annual Review of Earth and Planetary Sciences, v. 17, p. 89–118, doi:10.1146/annurev.ea.17.050189.000513.
Tada, R., Maliva R., and Siever, R., 1987, A new mechanism for pressure solution in porous quartzose sandstone: Geochimica et Cosmochimica Acta, v. 51, n. 9, p. 2,295–2,301, doi:10.1016/0016-7037(87)90282-1.
Thomson, A., 1959, Pressure Solution and Porosity, *in* Ireland H. A., editor, Silica in Sediments: Society of Economic Paleontologists and Mineralogists, Special Publication, v. 7, p. 92–110.
van Noort, R., Spiers, C. J., and Peach, C. J., 2007, Effects of orientation on the diffusive properties of fluid-filled grain boundaries during pressure solution: Physics and Chemistry of Minerals, v. 34, p. 95–112, doi: 10.1007/s00269-006-0131-9.
Walderhaug, O., and Bjørkum, P. A., 2003, The effect of stylolite spacing on quartz cementation in the lzlower Jurassic stø formation, southern Barents Sea: Journal of Sedimentary Research, v. 73, n. 2, p. 146–156, doi: 10.2110/jsr.2006.015.
Walderhaug, O., Oelkers, E. H., and Bjørkum, P. A., 2004, An Analysis of the Roles of Stress, Temperature, and pH in Chemical Compaction of Sandstones—Discussion: Journal of Sedimentary Research, v. 74, n. 3, p. 447–449, doi: 10.1306/092503740447.
Walderhaug, O., Bjørkum, P. A., and Aase, N. E., 2006, Kaolin-Coating of Stylolites, Effect on Quartz Cementation and General Implications for Dissolution at Mineral Interfaces: Journal of Sedimentary Research, v. 76, p. 234–243, doi: 10.2110/jsr.2006.015.
Wangen, M., 1998, Modeling porosity evolution and cementation of sandstones: Marine and Petroleum Geology, v. 15, p. 453–465, doi:10.1016/S0264-8172(98)00026-9.
Weyl, P. K., 1959, Pressure Solution and the Force of Crystallization—A Phenomenological Theory: Journal of Geophysical Research, v. 64, n. 11, p. 2,001–2,025.